Chemistry–A European Journal

Research Article
doi.org/10.1002/chem.202203441

Chemistry
Europe
European Chemical
Societies Publishing

www.chemeurj.org

Molecular Design and Crystal Chemistry of Polyfluorinated Naphthalene-bis-phenylhydrazimides with Superior Thermal and Polymorphic Stability and High Solution Processability

Vincenzo Mirco Abbinante,[a] Marco Zambra,[a] Gonzalo García-Espejo,[a] Candida Pipitone,[b] Francesco Giannici,[b] Silvia Milita,[c] Antonietta Guagliardi,*[d] and Norberto Masciocchi*[a]

Abstract: Naphthalene tetracarboxylic diimides (NDIs) are highly promising air-stable *n*-type molecular semiconductor candidates for flexible and cost-effective organic solar cells and thermoelectrics. Nonetheless, thermal and polymorphic stabilities of environmentally stable NDIs in the low-to-medium temperature regime ($< 300\,°C$) remain challenging properties. Structural, thermal, spectroscopic, and computational features of polyfluorinated NDI-based molecular solids (with up to 14 F atoms per NDI molecule) are discussed upon increasing the fluorination level. Slip-stacked arrangement of the NDI cores with suitable π–π stacking and systematically short interplanar distances (< 3.2 Å) are found. All these materials exhibit superior thermal stability (up to 260 °C or above) and thermal expansion coefficients indicating a response compatible with flexible polymeric substrates. Optical bandgaps increase from 2.78 to 2.93 eV with fluorination, while LUMO energy levels decrease down to -4.37 eV, as shown per DFT calculations. The compounds exhibit excellent solubility of 30 mg mL^{-1} in 1,4-dioxane and DMF.

Introduction

Electronic devices based on organic semiconductors have attracted a great deal of attention due to unique properties such as lightweight, flexibility, and cost-effective fabrication.[1–6] In this field, π-conjugated molecular materials have been the subject of intense investigations addressing the optimization of both *n*-type (electron transporting) and *p*-type (hole transporting) semiconductors.[7] Nonetheless, currently available *n*-type materials do not perform as efficiently as the *p*-type ones, a condition limiting potential advances in fields such as organic photovoltaics and thermoelectrics. The major issue with the poor charge mobility of *n*-type organic semiconductors is most likely attributed to insufficient ambient stability (that is reactivity with air and moisture). Poor crystallinity, grain boundaries and morphology of polycrystalline thin films (prepared by solution processing for cost-effective electronic device fabrication) have also been demonstrated to be critical issues.[8]

Among the *n*-type molecular semiconductors, symmetrically disubstituted naphthalene and perylene tetracarboxylic diimides (from here on, NDI and PDI, respectively), have played the prototypical role of optimal candidates, as they combine a large electronic affinity (EA), π-π intermolecular interactions and easy functionalization at either the aromatic core or side chains. For this class of semiconductors, molecular design has greatly contributed to fundamental advances (particularly in organic field-effect transistors - OFET) towards the improvement of ambient and chemical stability and the control of the supramolecular packing for device optimization.[9,10,11,12] As an example, functionalization with F, Br and CN residues (i.e., electron withdrawing groups, EW) has been one of the most effective strategies to raise EA above 4 eV (in the gas-phase) or, as alternatively and commonly reported, to lower the LUMO energy level of the neutral species below -4.0 eV. Worth to note, this is in the $-3.90/-4.50$ eV ideal recommended range which favors a higher environmental stability, since ultralow LUMOs (< -4.60 eV) are known to lead to material instability due to attack by weak nucleophiles, such as water.[13]

Similar molecular design concepts have been used to address other relevant properties (charge mobility, device fabrication and processing conditions, etc.) for many *n*-type NDI/PDI derivatives prepared with a large variety of branching

[a] Dr. V. M. Abbinante, Dr. M. Zambra, Dr. G. García-Espejo,
     Prof. N. Masciocchi
     Dipartimento di Scienza e Alta Tecnologia & To.Sca.Lab.
     INSTM Unit, Università dell'Insubria
     via Valleggio 11, 22100 Como (Italy)
     E-mail: norberto.masciocchi@uninsubria.it

[b] Dr. C. Pipitone, Prof. F. Giannici
     Dipartimento di Fisica e Chimica "Emilio Segrè"
     Università di Palermo
     viale delle Scienze, Ed. 17, 90128 Palermo (Italy)

[c] Dr. S. Milita
     Istituto per la Microelettronica e Microsistemi
     Consiglio Nazionale delle Ricerche
     via Gobetti 101, 40129 Bologna (Italy)

[d] Dr. A. Guagliardi
     Istituto di Cristallografia & To.Sca.Lab.
     INSTM Unit, Consiglio Nazionale delle Ricerche
     via Valleggio 11, 22100 Como (Italy)
     E-mail: antonella.guagliardi@ic.cnr.it

Chem. Eur. J. **2023**, *29*, e202203441 (1 of 11)

© 2022 Wiley-VCH GmbH

Chemistry–A European Journal

Research Article
doi.org/10.1002/chem.202203441

Chemistry Europe
European Chemical
Societies Publishing

residues.[8,14,15,16] Remarkably, many cases of derivatives with different alkyl substituents well-documented the differences of the electron mobility as the consequence of the optimized intermolecular interactions, or, in other words, of more suitable interplanar distances (and offsets) between π-π stacked parallel cores in the solid state. In contrast, the effect of branching bulky or flexible residues on the propensity to polymorphs formation[17,18,19,20] and on thermal stability remains a rather overlooked aspect in NDI/PDI studies, if compared to other essential properties, such as good electrical conductivity and low thermal conductivity. The interest in this regard is indeed rapidly raising since thermal stability and polymorphic versatility are known to be detrimental to devices function and are essential requirements for organic photovoltaics and thermo-electrics (OTEs).[21]

In our ongoing search for new *n*-type NDI derivatives exhibiting superior thermal and polymorphic stability (potential candidates for OTEs operating at low-to-medium temperatures, ≤ 300 °C), we have initially prepared and characterized *n*-alkyl substituted NDI derivatives with 4 to 10 carbon atom chains branching out from the NDI core at the imide positions.[18] Their thermal characterization manifested a rich polymorphic landscape (with phase transitions occurring even below 100 °C in the bulk) leading to somewhat irreproducible film deposition, an effect that was ascribed to the increased conformational freedom of the linear *n*-alkyl chains.[18] Accordingly, these soluble materials afforded highly crystalline powders and films, though often polyphasic.[14,15,16] Much higher thermal and polymorphic stabilities of imido/hydrazimido derivatives were expected and, indeed, obtained upon replacing *n*-alkyls chains with *N*-substituted aryl residues, from RT to well above 450 °C.[22] Quantum-mechanical calculations (by DFT) and cyclo-voltammetric (CV) measurements also revealed a significant lowering of the frontier orbital energies of the hydrazimido derivative (facilitating its use as an electron acceptor). Note

however that semiconductors with ultralow LUMOs (< −4.60 eV) show materials instability due to attack by weak nucleophiles, such as water, limiting the ideal LUMO values for *n*-type semiconductors to the −3.90/−4.50 eV range. Notwithstanding, the limited solubility in common organic solvents prevented the deposition (by drop casting or spin coating methods) of films of sufficient quality and thickness. Aiming at overcoming these major limitations displayed by aryl-based while simultaneously retaining chemical and thermal stability and further enhancing the *n*-type character, we eventually chose to modify the branching hydrazimido aryls by adding numerous EW groups (−F or −CF$_3$ residues) in the periphery of the molecules. This strategy was partially inspired by the work of Ajayakumar et al.,[23] where NDI derivatives were prepared as chromogenic molecular sensors. More specifically, the strategy presented in Ref. [23] significantly improved electron mobility and materials stability when *para*-substituted −CF$_3$, −OCF$_3$ and −SCF$_3$ benzylamine residues were attached to NDI cores.[24,25] Fluorination is also known to enhance both materials solubility in organic solvents (a critical issue in the non-fluorinated aryl-based NDI's) and hydrophobicity, through the partially inverted charge density distribution of polyfluoroaryls and the presence of C−H···F interactions in the solid state, making them distinct from the corresponding hydrocarbons.[26]

In the present work, we focus on highly fluorinated 1,4,5,8-naphthalenetetracarboxylic-bis-phenylhydrazimides. The investigated molecules contain the symmetrically substituted NDI core linked to two phenylhydrazimides residues each, as illustrated in Figure 1, where a labelling scheme (F3, F5, F7) recalling the degree of fluorination vs. the non-fluorinated precursor (F0) is used. While the syntheses of F3 and F5 are known from the Ajayakumar's work (and herein extended to the new F7 derivative), a comparative, in depth structural and thermal study of the entire sequence is missing. Based on (variable-temperature) X-ray diffraction, scanning calorimetry
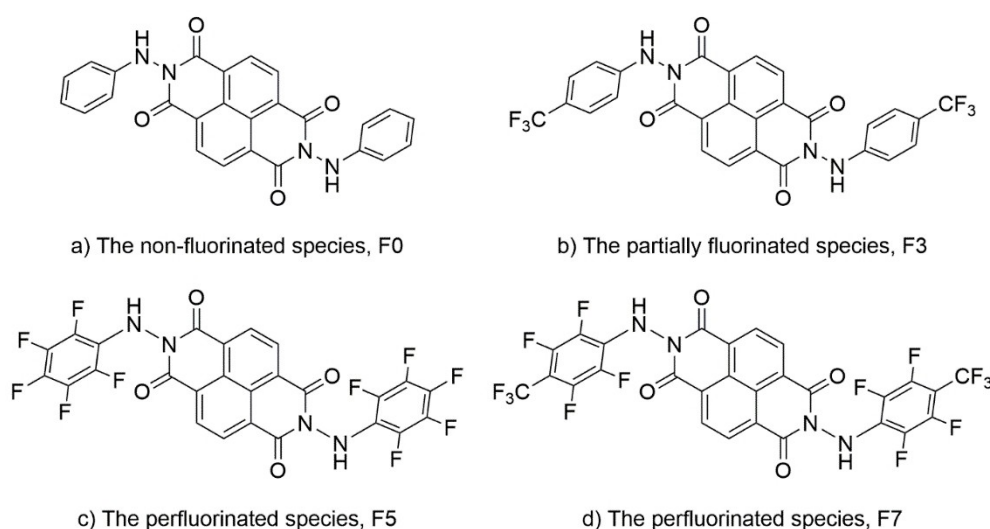

a) The non-fluorinated species, F0

b) The partially fluorinated species, F3

c) The perfluorinated species, F5

d) The perfluorinated species, F7

Figure 1. A sketch of the chemical structure of the non-fluorinated (F0) and fluorinated (F3, F5 and F7) molecules containing the NDI core substituted symmetrically linked to two phenylhydrazimides residues each.

Chemistry–A European Journal

Research Article
doi.org/10.1002/chem.202203441

**Chemistry
Europe**
European Chemical
Societies Publishing

and UV-Vis spectroscopy, we herein report a thorough solid-state characterization (in the powder form) and discuss the most relevant structural, polymorphic and optical band gap features, the superior thermal stability and highly improved room temperature solubility (in many organic solvents) as a function of the degree of fluorination. The structural study provides a molecular-level understanding of the supramolecular arrangement in these materials, such as i) the geometrical overlap of NDI cores in slip-stacked moieties and ii) the occurrence of significantly short intermolecular contacts, systematically observed in these polyfluorinated species. Additionally, we fully characterized their thermal behavior (including anisotropic lattice strain), where polymorphic transitions occur only at relatively high temperatures ($>260\,°C$). This thermal inertness and the easy solution processability may indeed favor semiconducting thin film deposition and their subsequent annealing in air, intended to improve crystallinity and, ultimately, functional performances. Finally, the influence of the degree of fluorination on the frontier molecular orbitals of the NDI-derivatives is discussed, based on density functional theory (DFT) calculations. Together with optical band-gaps estimation by UV-Vis spectroscopy, these simulations provide a more complete survey on these species and further envisage their potential use in optoelectronic (OFET) devices, one of the most productive fields of application of molecular semiconductors.

Results and Discussion

Comparative crystal chemistry: The four crystal phases isolated at room temperature (F0, F3, F5 and F7, referred to as α-phases, see below) crystallize in the triclinic or monoclinic systems and, invariably, show centrosymmetric molecules sitting on -1 symmetry sites (see Figure 2). Accordingly, only a few torsional angles (for the molecular conformations) and stereochemical descriptors (for the molecular stacking) need to be discussed. The molecular point symmetry excludes bowing or twisting of the NDI cores, which lie flat in the crystals and favor the formation of short (and periodic) molecular stacking. In all the investigated systems, infinite stacks of parallel molecules (Figure 2) provide an anisotropic supramolecular structure.

That the nearly ubiquitous parallel stacking of the NDI (and PDI) aromatic cores in the bulk solids (or in the films) is a necessary, but not sufficient, prerequisite to attain conducting, optical and emissive properties has received a widely shared consensus. As a noteworthy exception, a very recent paper highlighted that sterically induced deformations toward bent or twisted (scilicet highly contorted) PDI cores greatly enhance the performance of PDI-based devices.[27]

In the triclinic F3 species, all stacks within the entire crystal are parallel, whereas slightly differently oriented ladders can be evidenced in the monoclinic crystals (F5 and F7, see Supporting Information Figure S1). The (fluoro-)aromatic residues stick out laterally from the NDI cores and connect to neighboring stacks through less energetic contacts.

Table 1 contains the relevant geometrical values (defined and illustrated in Figure 3), which differentiate the molecular ladders, present in all studied species. Analogous values are reported also for two fluorinated benzyl congeners recently reported in the literature (the 4-trifluoromethyl and 4-trifluoromethylsulfide species, here labeled as $_cCF_3$ and $_cSCF_3$, respectively) and jointly discussed for comparison.[24,25]

Crystal packing (i.e., intermolecular) effects are likely driving the molecular conformations in the solids inserted in Table 1, particularly at the flexible N–X (τ_1) and X–Ar (τ_2) joints (X=N, C), where the occurrence of bonds of substantially single (and σ) character enables a relative freedom of these torsional angles.

Indeed, the τ_1 values fall in a (relatively) limited range ($\Delta\tau_1 \sim 19°$), whereas the τ_2 ones show a wider variability ($\Delta\tau_2 \sim 60°$), with the lowest values found for phenylhydrazines with H in *ortho* positions (F0 and F3), and significantly larger values in the presence of *ortho*-F atoms (F5 and F7). In $_cCF_3$ and $_cSCF_3$, τ_2 is even larger. These differences can be easily rationalized by the
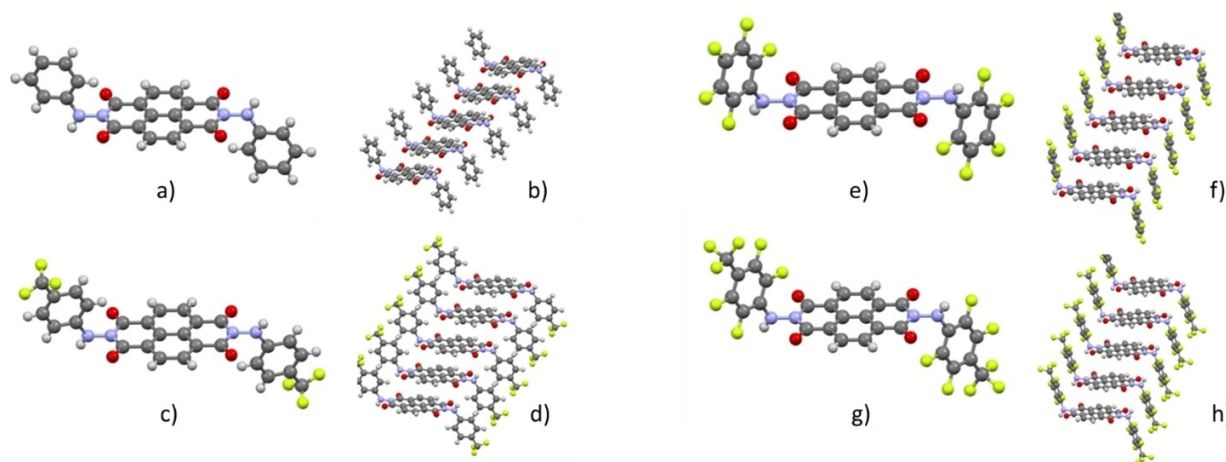

Figure 2. Molecular conformations and crystal packing in a ladder motif of the F0 (a,b), F3 (c,d), F5 (e,f) and F7 (g,h) molecules. Color codes for atoms: C (grey); H (white); N (blue), O (red) and F (yellow). NDI cores are iso-oriented to make comparisons easy.

Chem. Eur. J. **2023**, *29*, e202203441 (3 of 11)

© 2022 Wiley-VCH GmbH

Chemistry–A European Journal Research Article
doi.org/10.1002/chem.202203441

Chemistry
Europe
European Chemical
Societies Publishing

Table 1. Synoptic collection of the most relevant stereochemical descriptors for F0, F3, F5 and F7, together with those of the $_cCF_3$ and $_cSCF_3$ benzyl congeners. Values for the high-temperature γ-F5 phase, measured at 310 °C and later discussed, are also included.

Species	F0	F3	F5 (γ-F5)	F7	$_cCF_3$	$_cSCF_3$
τ_1, °	84.7	74.7	65.7 (69.7)	77.6	78.6	75.9
τ_2, °	7.7	18.8	59.1 (55.7)	51.4	63.7	66.9
χ, °	49.2	75.2	89.2 (80.0)	89.8	73.7	66.8
ψ, °	64.9	43.2	34.7 (43.3)	35.9	50.5	58.5
DoO	0.63	0.63	0.57 (0.63)	0.59	0.72	0.76
d, Å	3.38	3.06	3.01 (3.31)	3.18	3.42	3.51

τ_1 = torsion angle about the N–X (X = N, C, the hydrazido- (N) or benzylic (C) atoms of the branching aromatic residue); τ_2 = X–Ar (Ar = aryl) torsion angle. The stereochemical descriptors addressing the crystal packing of the molecular cores (χ, ψ, and d, shown in Figure 3) are defined in the main text and extensively discussed in Ref. [18]. Specifically, d is the length of the stacking vector projected onto the axis normal to the NDI core (z in Figure 3).

presence of NH···O intermolecular interactions in the phenyl-hydrazimides (leading to a face-to-face embrace across an inversion center in F3, and to a catemeric H-bond sequence winding up about a 2_1 axis in F5 and F7), which do not exist in the benzylic analogues.

The intermolecular stacking variability is herein addressed by the χ and ψ descriptors (the arguments of the direction cosines of the stacking vector - SV, the red arrow in Figure 3) quoted in Table 1, and by d (the projection of SV along the z axis). The χ, ψ descriptors have been introduced in our previous paper[18] for measuring (through the degree of overlap, $DoO = \sqrt[2]{1 - \cos^2\chi - \cos^2\psi}$) the superimposition (null or partial, for $0 < DoO < 1$, or complete, for $DoO = 1$) of neighboring NDI cores along the direction orthogonal to the NDI molecular plane. This geometrical descriptor is indeed partially correlated to the solid-state charge carrier mobility in organic semiconductors through intermolecular charge hopping. Worth of note, the eclipsed configuration $DoO = 1$ is energetically unfavored and limits charge transport,[28] whereas lower DoO values reflect slip-stacked arrangement of aromatic π-π interactions.[29] In this regard, a lower limit of $DoO = 0.53$ must be further considered, corresponding to an extremely slipped pair of NDI cores ($\chi = 90°, \psi = 32°$), where the two peripheral carbon atoms of HCCH connectivity (and different molecular

edges) are eclipsed. Values in Table 1 show that, in the solid state, all fluorinated compounds are significantly different from the pristine F0 one (χ and ψ become inverted). These values are more extreme for the perfluorinated F5 (in the α- and γ- forms) and F7 species, demonstrating that the number of fluorine substituents on the aromatic ring makes indeed some difference. In fact, F3, $_cCF_3$ and $_cSCF_3$, which only possess trifluoromethyls on the para-position residues, are much more similar one to each other, and fall in an intermediate χ, ψ class. Nonetheless, their NDI-core superimposition is only moderately affected: the DoO's remain in the 0.57-0.63 range (close to the 0.63 value of F0) and in line with values found in alkyl-based NDI-derivatives.[18]

More striking in this regard is the systematically low interplanar distance, d, of two stacked (but differently slipped) NDI cores within each π-π based ladder, falling in the 3.01–3.18 Å range for the three fluorinated hydrazimides F3, F5 and F7 solids (vs. 3.38 Å in F0). Beyond being related to the smaller size of N (vs. C) atoms in the core (as found for example in π-stacked N-rich aromatic compounds[30] and in line with Bondi's van der Waals radii[31]), this short interplanar distance (which is, per se, a pure geometrical feature) might also be favored by the partial depletion of the π-electrons from the NDI aromatic portion, less efficient in $_cCF_3$ and $_cSCF_3$ (with d values falling in the 3.42–3.51 Å range). This finding confirms how molecular/crystal packing design can be used to tailor and modify structural properties and, in a long term, also functional ones. It should be however noted that charge-transport properties depend on the structural ones in a very complex manner and that the electronic coupling of π-π stacked aromatic cores is still far to be modeled, and fully understood, though many computational efforts have been extensively used to partially address these aspects.[32] In this regard, two parameters are considered as most relevant: i) the transfer integral, which expresses the ease of transfer of a charge between two interacting moieties (through intermolecular charge hopping).[33] This is heavily dependent on the π-π distance, orientation and the relative displacement distance[34] (i.e., on those structural properties that are here inserted in Table 1); ii) the (less predictable) reorganization energy, which is related to the molecular degrees of freedom and is smaller in rigid than in flexible molecules. Since lower reorganization energies are
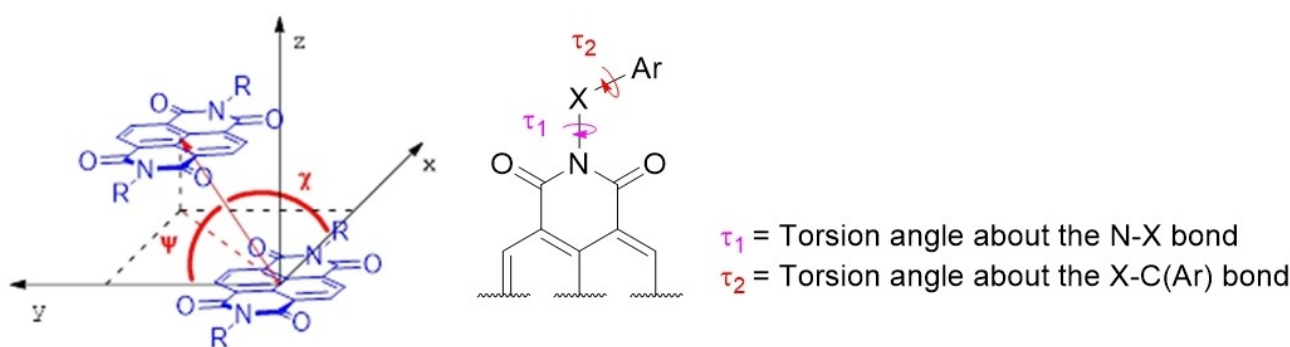

Figure 3. A sketch of the stereochemical descriptors (χ, ψ, left; τ_1, τ_2, right) collected in Table 1.

Chem. Eur. J. **2023**, *29*, e202203441 (4 of 11)

© 2022 Wiley-VCH GmbH

Chemistry–A European Journal

Research Article
doi.org/10.1002/chem.202203441

Chemistry
Europe
European Chemical
Societies Publishing

widely considered favorable for a high carrier mobility, the stiffness of molecules based on fluoroaromatics (as those studied in the present work) rather than fluoroalkyls, is therefore a promising feature for the investigated compounds.

Thermal properties: Variable temperature X-ray diffraction (VT-XRD) was used to follow the thermal stability and evolution of the different crystal phases. Substantial stability of the F3, F5 and F7 crystal phases is demonstrated in a wide temperature range, from RT to (at least) 250 °C (see Figure 4). A slightly higher stability is reported for the non-fluorinated F0 species which showed XRPD pattern constancy up to 300 °C (decomposition starts above 320 °C–TG/DSC evidence).[22] This behavior is herein paralleled by F3, which decomposes above 350 °C

without any preceding phase transition. In contrast, both F5 and F7 materials show more complex pathways, which were unveiled by coupling TG/DSC data with VT-XRD evidence.

Before decomposition (starting near 325 °C), two solid-state phase transitions are observed in F5, one at ca. 245 °C ($\alpha \rightarrow \beta$, $\Delta H = 4.2$ kJ mol^{-1}) and the other at 285 °C ($\beta \rightarrow \gamma$, $\Delta H = 10.3$ kJ mol^{-1}). Detecting the diffraction pattern of the β phase by VT-XRD proved to be very difficult, due to the large temperature gradient felt by the heated powders in contact with air. Its XRPD trace went however observed in one single experiment (see Figure S2), confirming its real (though transient) existence. While the β phase remains elusive, the XRPD pattern of γ-phase could be indexed from data collected at
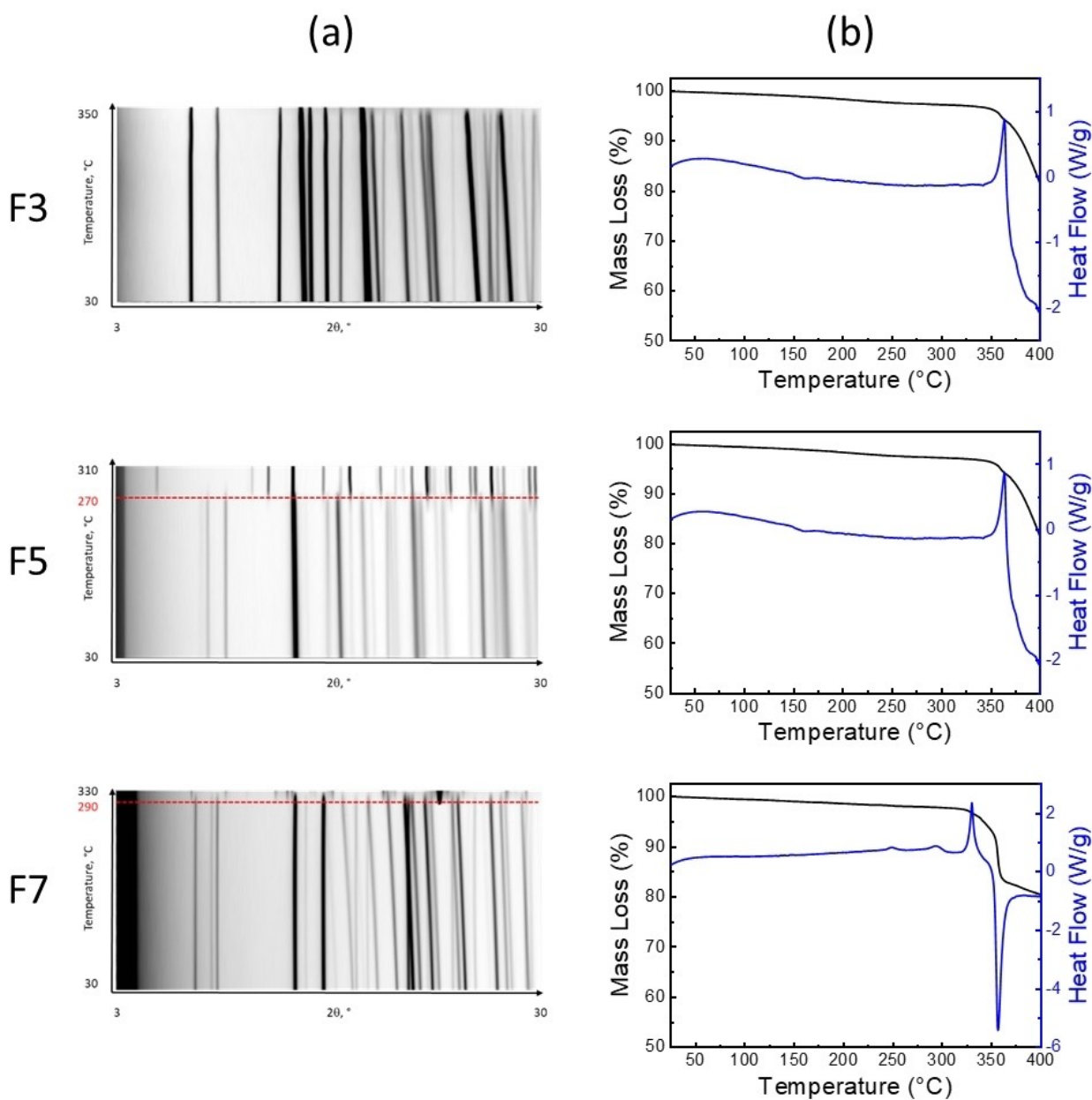

Figure 4. a) Variable temperature XRPD scans (3–30° 2θ range), from 30 °C (bottom) to 350, 310, and 330 °C, for F3, F5 and F7, respectively. The dotted red lines indicate the occurrence of solid-solid phase-transitions. b) The TG (black) and DSC (blue) traces, drawn in the 50–400 °C range.

Chemistry–A European Journal

Research Article
doi.org/10.1002/chem.202203441

Chemistry
Europe
European Chemical
Societies Publishing

Table 2. Thermal expansion coefficients κ_x for the axes lengths, interaxial angles and cell volume. The principal strain eigenvalues (E_i, i = 1,2,3, representing the thermal expansion coefficients along the principal axes) and the ϕ angles of the corresponding eigenvectors with the a, b, c axes, computed for a 100 °C increase from room temperature, are also reported.

Species	F0	α-F3	α-F5	α-F7
κ_a, MK^{-1}	38	22	21	27
κ_b, MK^{-1}	78	76	53	124
κ_c, MK^{-1}	16	65	42	21
κ_α, MK^{-1}		21		
κ_β MK^{-1}	−43	−46	6	10
κ_γ, MK^{-1}		−3		
κ_V, MK^{-1}	141	139	117	177
E_1	7	−6	45	19
E_2	70	58	22	34
E_3	75	86	45	133
ϕ_{E1} (a,b,c). °	129, 90, 33	140. 76. 63	11, 90, 76	53, 90, 27
ϕ_{E2} (a,b,c). °	141, 90, 123	124, 115, 135	79, 90, 166	143, 90, 63
ϕ_{E3} (a,b,c). °	90, 180, 90	72, 151, 50	90, 0, 90	90, 180, 90

Table 3. Solubility properties of the different NDI-bis-hydrazimides.

Species	Soluble in: (mg mL^{-1})	Insoluble in: (< 2 mg mL^{-1})
F0	chloroform (2), acetonitrile (2), tetrahydrofuran (4), N,N-dimethylformamide (30)	ethyl acetate, 1,4-dioxane, methanol, acetone, dichloromethane
F3	ethyl acetate (2), acetone (25) tetrahydrofuran (15), N,N-dimethylformamide (30)	chloroform, 1,4-dioxane, methanol
F5	ethyl acetate (2), acetone (2), tetrahydrofuran (25), N,N-dimethylformamide (30), 1,4-dioxane (30)	chloroform, toluene, ethanol, acetonitrile, diethyl ether, dichloromethane
F7	ethyl acetate (8), acetone (5), tetrahydrofuran (35), N,N-dimethylformamide (30), 1,4-dioxane (40)	chloroform, methanol, acetonitrile

Table 4. Optical E_{gap} energies calculated from Tauc plots (derived from UV-Vis reflectance spectra of the solid species) and HOMO-LUMO gaps computed with DFT and in Ref. [23]. All reported values are in eV.

	F0	α-F3	α-F5	α-F7
Optical E_{gap} (in the solid)	2.94	2.78	2.88	2.93
HOMO level	−6.26	−6.80	−7.07	−7.54
LUMO level	−3.98	−4.27	−4.22	−4.37
HOMO-LUMO gap	2.28	2.53	2.85	3.17
HOMO-LUMO gap (ref. [23])		2.6	3.3	

310 °C (see Supporting Information, Table ST1) and a sufficiently reliable structural model determined, based on the 5–30° 2θ portion of the pattern (limited by the high-temperature chamber). Figure S3 shows its conformation, with stacking and torsional values gathered in Table 1. Interestingly, we noticed from structural parameters in Table 1, that the α-F5 and γ-F5 show similar τ_1 and τ_2 torsional angles of the perfluorophenylhydrazimide residue, but a rather different stacking distance between the NDI cores, which rises from 3.01 to 3.31 Å upon crossing the phase-transition regime. Accordingly, also the stereochemical descriptors χ and ψ of the high-temperature phase are slightly different from those of α-F5 and move towards those of the non-ring fluorinated ones (F3, $_C$CF$_3$ and $_C$SCF$_3$) thus partially restoring more conventional packing features.

By cooling γ-F5 to RT within 30 min resulted in a polyphasic mixture of the pristine high-temperature phases with a new (previously undetected) ω-phase. Repeated measurements performed within a week showed the substantial constancy of the XRPD pattern of these mixtures, indicating the (partial) transformation to a more stable system. The persistent coexistence of both polymorphs at RT prevented a complete ω-F5 structural characterization, nevertheless, its reliable metrical characterization (by the structureless Le Bail refinement method, see Figure S4) was still possible, and is reported in Table ST1.

At variance, F7 shows only one pre-melting event (onset at 260 °C), characterized by a (still uninterpreted) $< 2.0\%$ weight loss and relatively large enthalpic change ($\Delta H = 12.2$ kJ mol^{-1}), with the resulting material (the β-F7 phase) still being crystalline. Also for this high temperature phase (visible in Figure 4 and, in more detail, in Figure S3) the XRPD pattern was indexed and the unit cell determined (see Table ST1). The cell metrics and space group symmetry clearly suggest that this structure is likely characterized by a Z′ = 1 value, while all other structures presented in this work show Z′ = 0.5. Jointly with the limited XRPD dataset available for the pure, monophasic β-F7 crystal phase, this makes the building of a suitable structural model a formidable, and still unsolved, task. Cooling β-F7 to room temperature provided a complex, unindexable XRPD trace, where neither α-F7 nor β-F7 patterns could be recognized, suggesting the formation of a polyphasic conglomerate of unknown polymorphic phases. Altogether, the thermal analysis of the three F3, F5 and F7 solids indicates that a higher degree of fluorination (as in F5 and F7) slightly lowers the thermal stability of the α-phases, with the formation of high-T polymorphs above 245 °C or so.

We also studied the heavily anisotropic thermal evolution of the lattice metrics for all F0, F3, F5, and F7 species and used Ohashi's method for determining the thermally induced
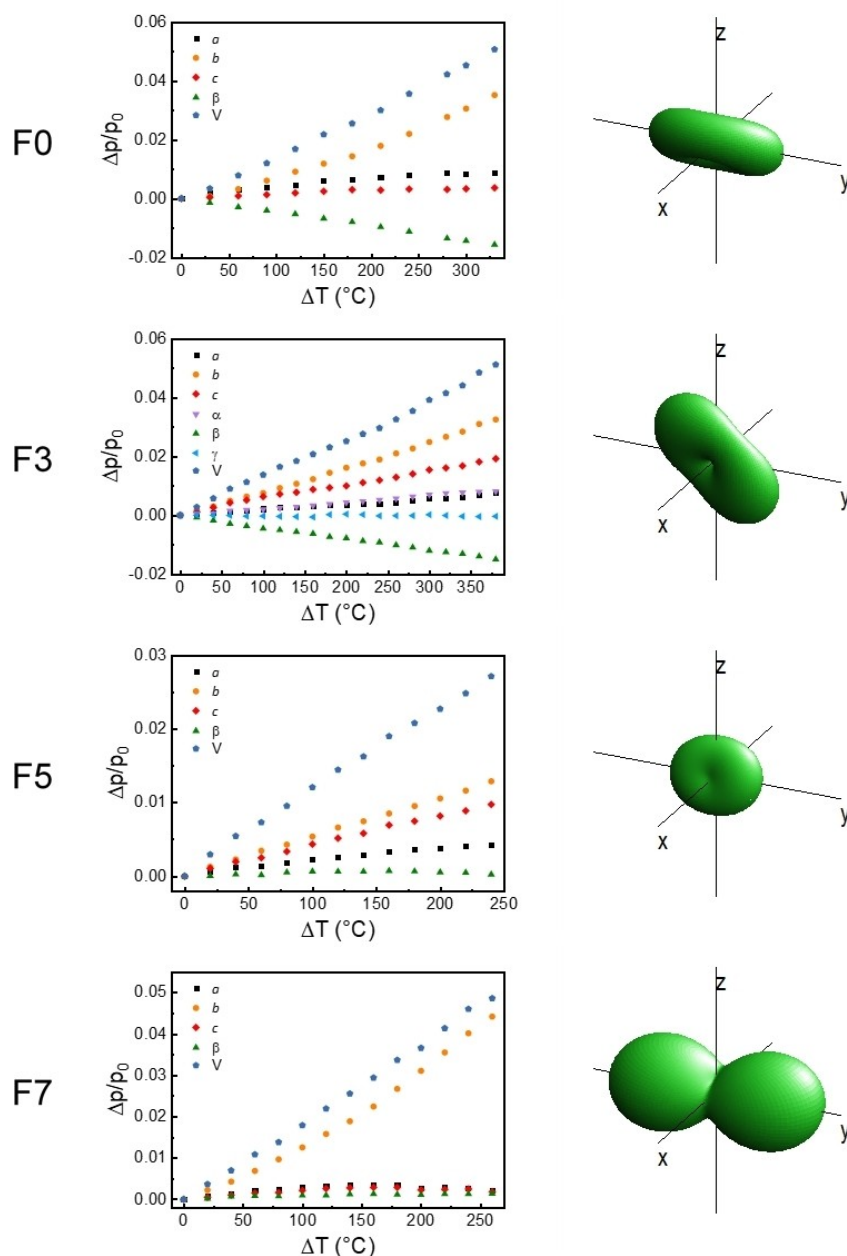
Chem. Eur. J. **2023**, *29*, e202203441 (6 of 11)

© 2022 Wiley-VCH GmbH

Figure 5. Left: plot of the $(x_T-x_{25})/x_{25}$ values vs. ΔT ($\Delta T = T\text{-}25\,°C$). Right: the corresponding strain tensors, drawn on the same absolute scale and computed using the 25–125 °C set of data.

strain[35] (as implemented in the Win_strain program[36]). We derived thermal expansion coefficients, including those of the principal axes, which help understanding (in the linear approximation, collected in Table 2) the full relative changes of the x parameters ($x = $a, b, c, α, β, γ and V), plotted in Figure 5 as $(x_T$-$x_{25})/x_{25}$, vs. ΔT ($\Delta T = $T-25 °C), and the full thermal tensors, graphically illustrated through Wintensor.[37] These studies indicate that all species have a predominant tendency to expand along the b axis (see κ_b values in Table 2), to an extent that is maximized in α-F7, for which the strain tensor shows the highest anisotropic shape. Table 2 also contains the linear thermal expansion coefficients of the principal axes, which help

understanding the size, shape and orientations of the tensors represented in Figure 5. That the maximum expansion direction is indeed the same in F0 and in the three fluorinated congeners is also manifested by the largest (E_3) eigenvalues, corresponding to eigenvectors aligned with **b** (see the ϕ_{E3} values in Table 2). Considering that in all phases the **b** axis corresponds to the shortest crystal periodicity (determined by the sequence of π-π contacts), we can safely attribute the thermally-induced lattice inflation to the relatively soft intermolecular interactions holding together the stacked cores, if compared to the Y···Y ones (Y = H, F).
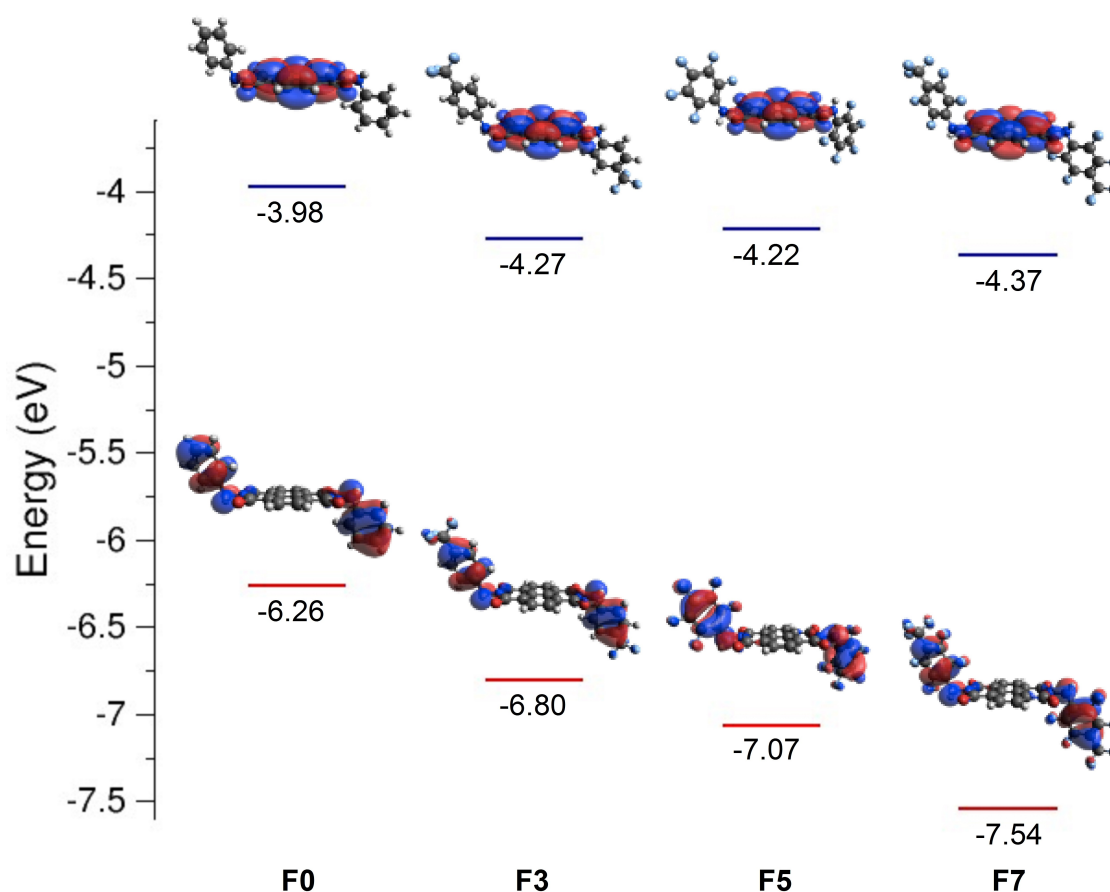
Figure 6. Energy scheme and the HOMO and LUMO isosurfaces for F0, F3, F5, and F7 (left to right).

The common thermal response behavior of all compounds is of high relevance if highly oriented thin films of these species are prepared with the stacking of NDI cores in an edge-on fashion, forming lamellar structures providing efficient charge mobility parallel to the substrate (larger than along its normal direction).[38,39] Indeed, in bottom gate OFET configurations, the ideal orientation of π-conjugated cores should be nearly perpendicular to the dielectric surface (edge-on arrangement) for efficient source to drain charge transport. The κ_b values of the F3, F5 and F7 solids, falling in the 54–124 MK^{-1} range (see Table 2), are much larger than those of a standard Si or SiO$_2$ substrate (a few units in MK^{-1} scale), but are fully compatible with flexible organic polymers, where linear thermal expansion coefficients fall in the 20–100 MK^{-1} range.[40]

Such similarity may indeed help in avoiding the formation of cracks or other macroscopic damages if films are deposited on plastic substrates and subsequently heated.

Solubility: As briefly mentioned in the introductory section, solution-processability is one of the most pursued organic semiconductor functions for cost-effective devices, and suitable strategies have been addressed to this scope. Herein, fluorination of the aromatic rings in the side chains was also intended as the strategy for improving the solubility of the high-thermally stable F3, F5, and F7 compounds.

Results of the solubility tests, performed at room temperature in many organic solvents, are synoptically collected in Table 3. As a rule, chloroform, dichloromethane, acetonitrile, and methanol demonstrated a poor aptitude in dissolving these species (<2 mg mL^{-1}), while 1,4-dioxane and N,N-dimethylformamide were the best performers (with solubilities as high as 40 mg mL^{-1}). Specifically, the limited solubility of F0 (which, inter alia, surpasses that of its configurational isomers with m- or p-diamino aryls[22]) is highly improved in the fluorinated derivatives when polar (but not protic) solvents are employed. This observation is in line with the more polar character of C–F bonds than C–H ones, both for the aliphatic and the aromatic fluorines.[41]

The high solubility in several solvents is therefore a promising feature for the development of simple solution-based film deposition strategies, which could not be achieved with similar NDI species bearing non-fluorinated aromatic imide residues.[22]

Spectroscopic characterization: UV-Vis spectroscopic measurements were performed (in reflectance conditions) on solid pressed powders. Figure S5 contains the reflectance-based Tauc plots (calculated for a direct-transition) and the related optical band gaps. The pertinent values are collected in Table 4.

The optical energy band-gaps in the F3, F5 and F7 sequence, progressively increase from 2.78 to 2.93 eV, as

Chemistry–A European Journal

Research Article
doi.org/10.1002/chem.202203441

Chemistry Europe
European Chemical
Societies Publishing

expected for the significant lowering of the HOMO level (centered on the NDI core, as supported by DFT calculations, see below). Such lowering is associated with the presence of EW groups and is accompanied by a more limited, but still significant, decrease of the LUMO energy.[12] Our DFT calculations and previously reported solution-phase cyclovoltammetric[42] and gas-phase computational[23] results coherently support this finding, though the optical gaps are surprisingly much more similar to each other than one could expect from computations. The relatively large gaps suggest that suitable strategies (doping,[43] or even self-doping[44]) have to be pursued for enhancing the functional properties of these materials (above all, electron conductivity) in the preparation of efficient films and devices.

As an alternative approach in the search of optimal *n*-type semiconductors for OTEs applications with lower gap, shifting to PDI-based aromatic cores, where functionalization by polyfluorinated aromatic residues is accompanied by the (relatively easy) insertion of –Br or –CN groups in the bay position, is also a strategy we intend to follow in future work.

Computational analysis: The ground state (GS) energies of the frontier molecular orbitals were calculated for gas-phase F0, F3, F5, and F7 (see Figure 6). As the Koopmans' theorem has been shown to hold well on various perylenediimide compounds,[45] these energies in the ground state may be regarded as representing the first ionization potential (defined as -HOMO energy) and the electron affinity, or reduction potential (defined as LUMO energy) of the isolated molecules reported in Table 4. This table includes for comparison also values from Ref. [23], computed using old ZINDO methods.

To help comparing our results with the reported values of other NDI derivatives, gathered in Ref. [46], the LUMO energy is calculated from the singlet GS. In large aromatic molecules, this level is often higher-lying (less negative) than the experimental data from electrochemistry, even by 1 eV.[47,48] Notably, through fluorination of the aromatic rings in the side chains, LUMO levels (down to −4.37 eV), as low as those obtained upon core functionalization, are found.[7]

It is worth noting that several effects were not accounted for in the simulations. Most importantly, the intermolecular interactions in the solid-state (π-π stacking, mainly) were neglected, and they are expected to be important in determining the electronic properties of the solid materials: for instance, valence bandwidths as large as 0.5–1 eV were predicted in crystalline substituted perylene diimides.[45] Another important aspect in the solid state is the possible dependence of the frontier orbitals energy on the dihedral angle between core and side rings, which is also determined by crystal packing interactions, absent in the gas-phase.

Conclusion

In this paper, we have presented the structural, thermal, spectroscopic, and computational characterization of three air-stable polyfluorinated naphthalene-tetracarboxylic bis-phenyl-hydrazimides and discussed the results in terms of a molecular

design approach towards higher thermal and polymorphic stability and increased solubility. The thermal inertness in the solid state is witnessed by the absence of polymorphic transitions, melting or chemical decomposition when heated up to 245 °C or more. The crystal structures of these solids, retrieved from laboratory X-ray powder diffraction data, indicate that the approach was successful in significantly shortening distances between the planes containing the stacked aromatic cores. This effect was rationalized by the presence of N and O (smaller than C) atoms, and possibly fostered by the simultaneous strong EW effect of the polyfluorinated branches, whereas fluorination only marginally influences the slip-stacked NDI core superimposition. This interpretation is indirectly supported by comparison to the structure of known benzylic congeners.

The solubility of these species was demonstrated to reach values as high as 30 mg mL^{-1} in 1,4-dioxane and DMF, solving the critical issue found in the non-fluorinated arylic analogues. This finding suggests the possibility of easy deposition of solution-processable thin films for a variety of applications. Experimentally measured optical band gaps indicate that fluorination of the branching phenyls is effective in modifying the electronic properties in the solid, where, upon increasing fluorination, E_{gap} increases as a consequence (rationalized by DFT calculations) of HOMO levels progressively lowered to a larger extent than LUMO levels. Work towards the preparation and optimization of thin films and the full characterization of their structural, morphological, and functional properties in OTE or OFET devices is in progress, which will be the subject of a forthcoming paper.

Experimental Section

Synthesis

Naphthalene-1,4,5,8-tetracarboxyl-bis-phenylhydrazimide (F0). The synthesis and characterization of F0 species was fully described in a recent paper of ours.[22]

Naphthalene-1,4,5,8-tetracarboxyl-bis-4-(trifluoromethyl)-phenylhydrazimide (F3), naphthalene-1,4,5,8-tetracarboxyl-bis-2,3,4,5,6-pentafluorophenylhydrazimide (F5) and naphthalene-1,4,5,8-tetracarboxyl-bis-2,3,5,6-tetrafluoro-4-(trifluoromethyl)-phenylhydrazimide (F7). The syntheses of these species were performed upon adoption of already known procedures.[23]

Physico-chemical characterization

Thermal analyses: Thermogravimetric (TG) and differential scanning calorimetry (DSC) traces were acquired from 30 to 400 °C (with a scan rate of 10 °C min^{-1}) using a Netzsch STA 409 PC Luxx® analyzer under a N_2 flow and with alumina sample holders equipped with a pierced lid.

UV-Vis Spectroscopy: UV-Vis reflectance spectra of the powders were acquired in the 200-900 nm range, using a UV-2600 Shimadzu spectrophotometer. $BaSO_4$ was used as reflectance standard and the measurements were performed on pelletized powders. The Kubelka-Munk function F[R] was calculated from reflectance spectrum R(E), where E is the photon energy, using the F[R] = (1-R)^2/2R relationship. Taking F[R] as representative of the sample

Chemistry–A European Journal

Research Article
doi.org/10.1002/chem.202203441

**Chemistry
Europe**
European Chemical
Societies Publishing

absorbance spectrum, extrapolation of the linear portion of the $(F[R]*E)^2$ vs. E on the E axis provided experimentally accessible optical direct band gap values.

Solubility tests: Powders of F0, F3, F5 and F7 species were dissolved at room temperature in the following organic solvents: methanol, ethanol, acetone, tetrahydrofuran, 1,4-dioxane, N,N-dimethylformamide, ethyl acetate, acetonitrile, toluene, dichloromethane and chloroform. Their maximum solubility was determined after vigorous stirring by observing the persistence of undissolved material. In a few cases, partial heating was necessary to increase dissolution rates; the determined solubility levels were however measured once solutions were cooled back to RT. The level of $2 \, mg \, mL^{-1}$ was chosen as an arbitrary threshold for separating the insoluble vs. soluble class of compounds.

X-ray Powder diffraction (XRPD): XRPD measurements were performed using a Bruker AXS D8 Advance diffractometer in Bragg-Brentano $\theta{:}\theta$ geometry, equipped with a Lynxeye position sensitive detector. DS: 0.5°; Generator setting: 40 kV, 40 mA; Ni-filtered Cu-K$_\alpha$ radiation, $\lambda = 1.5418$ Å. XRPD data for structure solution were collected in the 3–105° 2θ range for all samples, sampling at 0.02°, with scan time lasting ca. 16 h.

Variable temperature XRPD analysis (VT-XRPD): Variable temperature XRPD experiments were performed from 30 to 400 °C, or slightly beyond, to assess thermal and polymorphic stability. Powdered batches were deposited in the hollow of an aluminum sample holder of a custom-made heating stage (Officina Elettrotecnica di Tenno, Ponte Arche, Italy). Diffractograms were acquired in air, in the most significant (low-angle) 3–30° 2θ range, under isothermal conditions in 20 °C steps. Since in powder diffraction experiments the samples are in direct contact with the air and some thermal drifts/gradients are present, the accurate transition temperatures are calibrated on TG/DSC measurements.

Ab-initio crystal structure solution from X-ray diffraction data

XRPD structure solution of the F3, F5, and F7 phases was performed using the TOPAS-R[49] software. Standard peak search methods followed by profile fitting allowed the accurate estimate of the low-angle peak position. These values, through the SVD indexing algorithm,[50] provided primitive triclinic or monoclinic cells [a = 4.81, b = 11.23, c = 12.51 Å, $\alpha = 111.1°$, $\beta = 78.6°$, $\gamma = 102.8.4°$, GOF(20) = 46.4 for F3; a = 17.31, b = 5.29, c = 12.09 Å, $\beta = 87.6°$, GOF(20) = 15.0 for F5; a = 21.07, b = 5.41, c = 11.88 Å, $\beta = 113.9°$, GOF(20) = 45.0 for F7]. Space group determination through the analysis of systematic absences (after cell reduction and axis reorientation – i.e. forcing the shortest axis in b in all these species) indicated, for the three phases, P-1, $P2_1/n$, and $P2_1/n$, respectively, later confirmed by successful structure solution and refinement. Density considerations enabled the determination of the molecular symmetry, the Z' value and the content of the asymmetric unit. Structure solution of the three molecular crystals was performed by Monte Carlo/Simulated Annealing technique using a rigid model (flexible at the imide link) described by the Z-matrix formalism with standard geometrical parameters. The final refinements were eventually carried out by the Rietveld method, maintaining the rigid bodies introduced at the structure solution stage. Relaxing the constraints on the ideal $D2_h$ symmetry of the NDI core in F5 resulted, as expected, in very small aromatic CCCC torsional angles (well below 3°) with a marginally lower profile agreement factor (0.0677 vs. 0.0681). Considering that a CSD search (November 2022 version) provided 906 crystal structures in which torsional angles of the aromatic portion showed a narrow distribution, only 2.5° wide, we rejected this more complex model, and maintained the original symmetric description. The background was modelled by a polynomial function of the Chebyshev type, peak profiles were described by the Fundamental Parameters Approach[51] and a common (refinable) isotropic thermal factor was attributed to all atoms. March-Dollase correction for preferred orientation[52] was applied in the form of second order spherical harmonics. No attempt was tackled in determining, nor in refining, possible multiple orientations of the CF$_3$ group in F3 and F7, though single crystal studies revealed its tendency to be disordered in two, or more, positions.[53] Fractional atomic coordinates and crystal structure details were deposited with the CCDC.

Deposition Numbers 2183396 (F3), 2183397 (F5), and 2183398 (F7) contain the supplementary crystallographic data for this paper. These data are provided free of charge by the joint Cambridge Crystallographic Data Centre and Fachinformationszentrum Karlsruhe Access Structures service. Figure S6 contains the final Rietveld refinement plots. Specific sample-dependent issues are discussed in the Results section.

Crystal data for F3: $C_{28}H_{14}F_6N_4O_4$, fw = 584.42 g mol^{-1}, triclinic, P-1, a = 11.239(1), b = 4.8117(3), c = 12.523(1) Å, $\alpha = 101.374(4)$ °, $\beta = 68.903(3)$ °, $\gamma = 102.788(8)$ °, V = 611.0(1) Å^3, Z = 1, $\rho_{calc} = 1.588$ g cm^{-3}, $\mu(Cu\text{-}K_\alpha) = 12.1$ cm^{-1}; R_p and R_{wp}, 0.077 and 0.104 respectively, 7–105° 2θ range. $R_{Bragg} = 0.054$.

Crystal data for F5: $C_{26}H_6F_{10}N_4O_4$, fw = 628.33 g mol^{-1}, monoclinic, $P2_1/n$, a = 17.351(1), b = 5.2952(4), c = 12.1151(9) Å, $\beta = 87.600(6)$ °, V = 1112.1(1) Å^3, Z = 2, $\rho_{calc} = 1.876$ g cm^{-3}, $\mu(Cu\text{-}K_\alpha) = 16.6$ cm^{-1}, g(100) = 1.05; R_p and R_{wp}, 0.049 and 0.068 respectively, 5–105° 2θ range. $R_{Bragg} = 0.038$.

Crystal data for F7: $C_{28}H_6F_{14}N_4O_4$, fw = 728.35 g mol^{-1}, monoclinic, $P2_1/n$, a = 19.650(1), b = 5.4168(3), c = 11.8904(6) Å, $\beta = 79.803(3)$ °, V = 1245.6(1) Å^3, Z = 2, $\rho_{calc} = 1.942$ g cm^{-3}, $\mu(Cu\text{-}K_\alpha) = 18.3$ cm^{-1}, R_p and R_{wp}, 0.036 and 0.051 respectively, 7–105° 2θ range. $R_{Bragg} = 0.044$.

Computational methods

Ab initio density functional theory (DFT) was used to describe the ground state electronic structures on fully relaxed geometries imposing C_i point group symmetry. All the calculations were performed in the gas phase with Gaussian16,[54] using the B3LYP hybrid functional,[55,56] which is widely reported to be a good choice for the description of both ground and excited states in most cases.[57] The 6-31G+(d) basis set was chosen as a compromise between accuracy and calculation time since a preliminary test on F0 confirmed that the results were indistinguishable from 6-31G++(d,p).

Conflict of Interest

The authors declare no conflict of interest.

Chem. Eur. J. **2023**, *29*, e202203441 (10 of 11)

© 2022 Wiley-VCH GmbH

Data Availability Statement

The data that support the findings of this study are available in the supporting material of this article.

[1] *Organic Electronics: Emerging Concepts and Technologies*, (Eds. F. Cicoira, C. Santato), Wiley, New York, 2013.

[2] *Organic Electronics Materials and Devices*, (Ed. S. Ogawa), Springer, Tokyo, 2015.

[3] *Handbook of Flexible Organic Electronics, Materials, Manufacturing and Applications*, (Ed. S. Logothetidis), Woodhead Pub Ltd, Sawston, 2014.

[4] *The WSPC Reference on Organic Electronics: Organic Semiconductors*, (Eds. J. L. Brédas, S. R. Marder), World Scientific Publishing, Singapore, 2016.

[5] *Organic Flexible Electronics: Fundamentals, Devices, and Applications*, 1st edition (Eds. P. Cosseddu, M. Caironi), Woodhead Pub Ltd, Sawston, 2020.

[6] Y. Bonassieux, C. J. Brabec, Y. Cao, T. Breen Carmichael, M. L. Chabinyc, K.-T. Cheng, G. Cho, A. Chung, C. L. Cobb, A. Distler, H.-J. Egelhaaf, G. Grau, X. Guo, G. Haghiashtiani, T.-C. Huang, M. M. Hussain, B. Iniguez, T.-M. Lee, L. Li, Y. Ma, D. Ma, M. C. McAlpine, T. N. Ng, R. Österbacka, S. N. Patel, J. Peng, H. Peng, J. Rivnay, L. Shao, D. Steingart, R. A. Street, V. Subramanian, L. Torsi, Y. Wu, *Flex. Print. Electr.* 2022, *6*, 023001.

[7] J. Dhar, U. Salzner, S. Patil, *J. Mater. Chem. C* 2017, *5*, 7404–7430.

[8] C. D. Dimitrakopoulos, D. J. Mascaro, *IBM J. Res. Dev.* 2001, *45*, 11–27.

[9] A. Welford, S. Maniam, E. Gann, X. Jiao, L. Thomsen, S. J. Langford, C. R. McNeill, *Org. Electron.* 2019, *75*, 105378.

[10] N. N. Kolhe, T. Nandini Devi, S. P. Senanayak, B. Jancy, K. S. Narayan, S. K. Asha, *J. Mater. Chem.* 2012, *22*, 15235–15246.

[11] X. Fang, H. Ke, L. Li, M.-J. Lin, *Dyes Pigm.* 2017, *145*, 469–475.

[12] G. Gogoi, L. Bhattacharya, S. R. Sahoo, S. Sahu, N. Sen Sarma, S. Sharma, *RSC Adv.* 2021, *11*, 57–70.

[13] X. Guo, A. Facchetti, T. J. Marks, *Chem. Rev.* 2014, *114*, 8943–9021.

[14] N. Sakai, J. Mareda, E. Vauthey, S. Matile, *Chem. Commun.* 2010, *46*, 4225–4237.

[15] M. Al Kobaisi, S. V. Bhosale, K. Latham, A. M. Raynor, S. V. Bhosale, *Chem. Rev.* 2016, *116*, 11685–11796.

[16] S. Kumar, J. Shukla, J. Kumar, P. Mukhopadhyay, *Org. Chem. Front.* 2018, *5*, 2254–2276.

[17] H. Chung, S. Chen, B. Patel, G. Garbay, Y. H. Geerts, Y. Diao, *Cryst. Growth Des.* 2020, *20*, 1646–1654.

[18] S. Milita, F. Liscio, L. Cowen, M. Cavallini, B. A. Drain, T. Degousée, S. Luong, O. Fenwick, A. Guagliardi, B.C. Schroeder, N. Masciocchi, *J. Mater. Chem. C* 2020, *8*, 3097–3112.

[19] F. Marin, S. Tombolesi, T. Salzillo, O. Yaffe, L. Maini, *J. Mater. Chem. C* 2022, *10*, 8089–8100.

[20] I. De Oliveira Martins, F. Marin, E. Modena, *Faraday Discuss.* 2022, *235*, 490–507.

[21] B. Russ, M. J. Robb, F. G. Brunetti, P. Levi Miller, E. E. Perry, S. N. Patel, V. Ho, W. B. Chang, J. J. Urban, M. L. Chabinyc, C. J. Hawker, R, A. Segalman, *Adv. Mater.* 2014, *26*, 3473–3477.

[22] V. M. Abbinante, G. García-Espejo, G. Calabrese, S. Milita, L. Barba, D. Marini, C. Pipitone, F. Giannici, A. Guagliardi, N. Masciocchi, *J. Mater. Chem. C* 2021, *9*, 10875–10888.

[23] M. R. Ajayakumar, P. Mukhopadhyay, *Chem. Commun.* 2009, 3702–3704.

[24] H. E. Katz, T. Siegrist, J. H. Schön, Ch. Kloc, B. Batlogg, A. J. Lovinger, J. Johnson, *ChemPhysChem.* 2001, *3*, 167–171.

[25] L. Zhao, D. Zhang, Y. Zhu, S. Peng, H. Meng, W. Huang, *J. Mater. Chem. C* 2017, *5*, 848–853 and references therein.

[26] F. Babudri, G. M. Farinola, F. Naso, R. Ragni, *Chem. Commun.* 2007, 1003–1022.

[27] C. Schaak, A. M. Evans, F. Ng, M. L. Steigerwald, C. Nuckolls, *J. Am. Chem. Soc.* 2022, *144*, 42–51.

[28] N. Renaud, P. A. Sherrat, M. A. Tattner, *J. Phys. Chem. Lett.* 2013, *4*, 1065–1069.

[29] P. E. Hartnett, A. Timalsina, H. S. S. R. Matte, N. Zhou, X. Guo, W. Zhao, A. Facchetti, R. P. H. Chang, M. C. Hersam, M. R. Wasielewski, T. J. Marks, *J. Am. Chem. Soc.* 2014, *136*, 16345–16356.

[30] R. Centore, M. Causà, S. Fusco, A. Carella, *Cryst. Growth Des.* 2013, *13*, 3255–3260.

[31] A. Bondi, *J. Phys. Chem.* 1964, *68 (3)*, 441–451.

[32] See for example: J. L. Bredas, J. P. Carbert, D. A. da Silva-Filho, J. Cornil, *PNAS* 2002, *99*, 5804–5809, and references therein.

[33] Y. Olivier, V. Lemaur, J. L. Brédas, J. Cornil, *J. Phys. Chem. A* 2006, *110*, 6356–6364.

[34] K. J. Thorley, C. Risko, *J. Mater. Chem. C.* 2016, *4*, 3825–3832.

[35] Y. Ohashi, A program to calculate the strain tensor from two sets of unit-cell parameters, in *Comparative Crystal Chemistry*, (Eds. R. M. Hazen and L. W. Finger), Wiley, New York, 2002, 92–102.

[36] R. Angel, Win strain, www.rossangel.com/text_strain.htm, (accessed December 3rd, 2022).

[37] W. M. Kaminsky, Wintensor: Tensor-drawing and calculation tool for Windows 95/98/NT/2000/XP, https://cad4. cpac.washington.edu/Win-Tensorhome/WinTensor.htm (accessed December 3rd, 2022).

[38] A. Facchetti, M. Mushrush, M.-H. Yoon, G. R. Hutchison, M. A. Ratner, T. J. Marks, *J. Am. Chem. Soc.* 2004, *126*, 13859–13874.

[39] F. Liscio, S. Milita, C. Albonetti, P. D'Angelo, A. Guagliardi, N. Masciocchi, R. G. Della Valle, E. Venuti, A. Brillante, F. Biscarini, *Adv. Funct. Mater.* 2012, *22*, 943–953.

[40] *Polymer Handbook* (J. Brandrup, E. H. Immergut, E. A. Grulke, Eds.), Wiley, New York, 1999.

[41] D. O'Hagan, *Chem. Soc. Rev.* 2008, *37*, 308–319.

[42] M. R. Ajayakumar, G. Hundal, P. Mukhopadhyay, *Chem. Commun.* 2013, *49*, 7684–7686.

[43] A. Werner, F. Li, K. Harada, M. Pfeiffer, T. Fritz, K. Leo, S. Machill, *Adv. Funct. Mater.* 2004, *14*, 255–260.

[44] L. M. Cowen, J. Atoyo, M. J. Carnie, D. Baran, B. C. Schroeder, *ECS J. Solid State Sci. Technol.* 2017, *6*, N3080-N3088.

[45] M. C. Ruiz Delgado, F. C. Kim, D. A. da Silva Filho, J. L. Brédas, *J. Am. Chem. Soc.* 2010, *132*, 3375–3387.

[46] F. N. Miros, S. Matile, *Chem. Open* 2016, *5*, 219–226.

[47] M. Pastore, S. Fantacci, F. De Angelis, *J. Phys. Chem. C* 2010, *114*, 22742–22750.

[48] T. M. McCormick, C. R. Bridges, E. I. Carrera, P. M. DiCarmine, G. L. Gibson, J. Hollinger, L. M. Kozycz, D. S. Seferos, *Macromol.* 2013, *46*, 3879–3886.

[49] TOPAS–R, V. 3.0, Bruker AXS, Karlsruhe, Germany, 2005.

[50] A. A. Coelho, *J. Appl. Crystallogr.* 2003, *36*, 86–95.

[51] R. W. Cheary, A. Coelho, *J. Appl. Crystallogr.* 1992, *25*, 109–121.

[52] W. A. Dollase, *J. Appl. Crystallogr.* 1986, *19*, 267–272.

[53] P. Müller, *Crystallogr. Rev.* 2009, *15*, 57–83.

[54] M. J. Frisch, G. W. Trucks, H. B. Schlegel, G. E. Scuseria, M. A. Robb, J. R. Cheeseman, G. Scalmani, V. Barone, G. A. Petersson, H. Nakatsuji, X. Li, M. Caricato, A. V. Marenich, J. Bloino, B. G. Janesko, R. Gomperts, B. Mennucci, H. P. Hratchian, J. V. Ortiz, A. F. Izmaylov, J. L. Sonnenberg, D. Williams-Young, F. Ding, F. Lipparini, F. Egidi, J. Goings, B. Peng, A. Petrone, T. Henderson, D. Ranasinghe, V. G. Zakrzewski, J. Gao, N. Rega, G. Zheng, W. Liang, M. Hada, M. Ehara, K. Toyota, R. Fukuda, J. Hasegawa, M. Ishida, T. Nakajima, Y. Honda, O. Kitao, H. Nakai, T. Vreven, K. Throssell, J. A. Jr. Montgomery, J. E. Peralta, F. Ogliaro, M. J. Bearpark, J. J. Heyd, E. N. Brothers, K. N. Kudin, V. N. Staroverov, T. A. Keith, R. Kobayashi, J. Normand, K. Raghavachari, A. P. Rendell, J. C. Burant, S. S. Iyengar, J. Tomasi, M. Cossi, J. M. Millam, M. Klene, C. Adamo, R. Cammi, J. W. Ochterski, R. L. Martin, K. Morokuma, O. Farkas, J. B. Foresman, D. J. Fox, Gaussian 16, Revision C.01, Gaussian, Inc., Wallingford CT, 2016.

[55] A. D. Becke, *J. Chem. Phys.* 1993, *98*, 5648–5652.

[56] P. J. Stephens, F. J. M. Devlin, C. F. Chabalowski, M. J. Frisch, *J. Chem. Phys.* 1994, *98*, 11623–11627.

[57] C. Adamo, D. Jacquemin, *Chem. Soc. Rev.* 2013, *42*, 845–856.